Mechanical forcing of the North American monsoon by orography

(Article begins on next page)

25 July 2024

Mechanical forcing of the North American monsoon by orography

WILLIAM R. BOOS [1,2] AND SALVATORE PASCALE[3]

[1] *Department of Earth and Planetary Science, University of California, Berkeley, USA*
[2] *Climate and Ecosystem Sciences Division, Lawrence Berkeley National Laboratory, USA*
[3] *Department of Physics and Astronomy, University of Bologna, Italy*

ABSTRACT

A band of intense rainfall extends more than 1,000 km along Mexico's west coast during northern hemisphere summer, constituting the core of the North American monsoon[1;2]. As in other tropical monsoons, this rainfall maximum is commonly thought to be thermally forced by emission of heat from land and elevated terrain into the overlying atmosphere[3;4;5], but a clear understanding of the fundamental mechanism governing this monsoon is lacking. Here we show that the core North American monsoon is generated when Mexico's Sierra Madre mountains deflect the extratropical jet stream toward the equator, mechanically forcing eastward, upslope flow that lifts warm and moist air to produce convective rainfall. These findings are based on analyses of dynamic and thermodynamic structures in observations, global climate model integrations, and adiabatic stationary wave solutions. Land surface heat fluxes do precondition the atmosphere for convection, particularly in summer afternoons, but these heat fluxes alone are insufficient for producing the observed rainfall maximum. Our results indicate that the core North American monsoon should be understood as convectively enhanced orographic rainfall in a mechanically forced stationary wave, not as a classic, thermally forced tropical monsoon. This has implications for the response of the North American monsoon to past and future global climate change, making trends in jet stream interactions with orography of central importance.

CURRENT UNDERSTANDING OF THE MONSOON

Tropical monsoons occur when a surface of low heat capacity transfers the energy of intense summer solar radiation to the overlying atmosphere, creating thermally direct, precipitating flow. Such circulations supply water to billions of people and set the climate of large swaths of Earth's surface. The North American monsoon (NAM) is commonly viewed in this paradigm, being a low-latitude summer circulation crucial for the hydrology of western Mexico and the southwestern US[6;7;1;2].

Orography strongly alters this simple description of monsoons, with the core NAM consisting of a narrow tongue of high precipitation stretching over 1,000 km north-south just west of the Sierra Madre Occi-

Corresponding author: William R. Boos
billboos@alum.mit.edu

dental (SMO) mountains (Fig. 1a; summer means are taken July-September). The mechanisms that organize NAM precipitation around orography remain unclear, but most hypotheses invoke thermal forcing from terrain. Early global climate model (GCM) simulations showed that NAM rainfall decreases greatly when mountains are flattened globally[8], perhaps because sensible heat fluxes from orography into elevated levels of the atmosphere draw water vapor from the Gulf of California up SMO slopes to condense and precipitate[3;9;10;2].

The high-amplitude diurnal cycle of precipitation in the NAM has also been taken to suggest the importance of orographic thermal forcing, with near-surface air flowing upslope during daytime and downslope at night[11;12;13], as expected for a sea breeze or mountain-valley breeze driven by solar heating. Despite the prominence of this diurnal cycle, horizontal moisture fluxes produced by transients (e.g., diurnally reversing sea breeze circulations) are an order of magnitude smaller
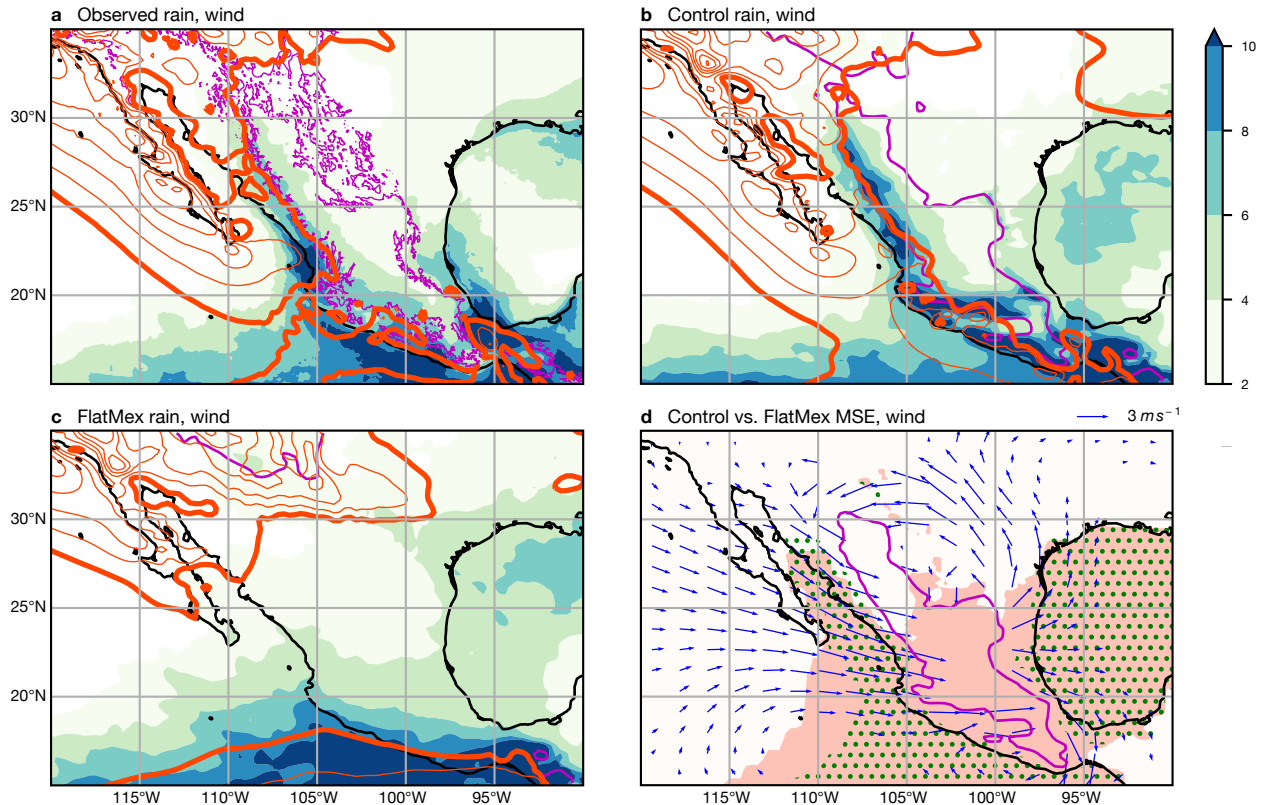
Figure 1. Influence of orography on rain and low-level wind. Summer (July-September) precipitation (shading, mm day^{-1}) and near-surface eastward wind (orange contours, interval 1 m s^{-1}, with zero contour bold and negative values omitted) for (a) observations, (b) the control GCM, and (c) the GCM with flattened orography over Mexico. Panel (d) shows anomalous 700 hPa horizontal wind (vectors) produced by Mexico's orography in the GCM, and the extent of the region with high surface air moist static energy (defined as a 2-meter value larger than 345 K) in the control model (green stippling) and the model with flattened orography over Mexico (red shading). Surface height of 1.5 km is contoured in magenta in all panels, and vectors in (d) are plotted only when either the zonal or meridional component passes a Student t-test at the 5% level. Mapping software: Cartopy with Natural Earth shapefiles.

in the core NAM than those produced by seasonal mean winds[12], suggesting that core NAM precipitation is controlled by the forcings that produce seasonal mean flow.

Mechanical, rather than thermal, effects of orography are known to drive summer winds east and northeast of the NAM, in the central US. A GCM and stationary wave model were used to show that the eastern Sierra Madre deflect trade winds northward to become the Great Plains low level jet[14;15], which transports water into the central US from the Gulf of Mexico but is not traditionally seen as a main NAM component. Both orographic elevated heating and orographic blocking of zonal winds have been mentioned as plausible NAM causes[16], but models integrated at resolutions fine enough to resolve the SMO[17;18;19] have not been used to distinguish between these possibilities.

Our goal is to determine the mechanisms that cause the intense rainfall maximum in the core NAM. Is it generated primarily by a thermodynamic forcing (e.g.

elevated heating) or a mechanical one (mechanical blocking)? Given the prior finding that time-mean vertically integrated moisture flux convergence in the core NAM is produced by time-mean winds[12], this task amounts to determining the cause of seasonal-mean eastward, upslope flow over the SMO.

NET RESPONSE TO OROGRAPHY

We integrate a high-resolution (0.25°-grid spacing) GCM twice: once with observed orography (Control) and again with surface height set to zero over most of Mexico (FlatMex). The Control integration produces a realistic seasonal cycle and spatial pattern of NAM precipitation and wind (Fig. 1a, b and Extended Data Figs. 1-3; the model has a positive precipitation bias but falls in the range of observed interannual variability). As in observations[12], model NAM precipitation is balanced by moisture converged by time-mean flow, with tran-

sients producing some compensating drying (Extended Data Fig. 4).

The model resolves the SMO as a ~3 km-high ridge along Mexico's west coast, and reproduces observed eastward low-level winds extending roughly 1000 km west of that (Fig. 1a, b). This wind distribution is suggestive of the midlatitude eastward jet being deflected toward the equator by the SMO; the broader North American cordillera is known to deflect the jet in such a stationary wave[14], but the equatorial part of that wave has not been argued to play a role in the NAM, nor adequately resolved in stationary wave models of the region.

We obtain the net response to all dynamic and thermodynamic effects of Mexico's orography by subtracting the FlatMex state from the Control. Nearly all core NAM precipitation is caused by local orography, with the rainfall maximum on Mexico's west coast disappearing in the FlatMex state despite continued land surface thermal forcing (Fig. 1c). Without the SMO, westward trade winds span Mexico, separating two zones of eastward flow: one in the extratropics and another in the oceanic intertropical convergence zone (ITCZ) south of Mexico (near 15°N). The region of high near-surface moist static energy (MSE), which in observations and the Control is confined to the Gulf of California and the Gulf of Mexico, expands inland to cover central Mexico when orography is flattened (Fig. 1d; surface air MSE is hereafter written h_s and expressed in temperature units through normalization by the specific heat of air).

The h_s response to the SMO suggests that core NAM precipitation is not forced primarily by orographic elevated heating, which would drive the overlying atmosphere toward higher h_s values than would be achieved over the same surface at sea level[20]. Additionally, the dynamical response to tropical heatings typically includes poleward flow through the heated region in a state of Sverdrup balance, with a low-level cyclone to the west[21,22]. Instead, we see anomalous eastward flow over the orographic forcing, with a low-level cyclone to the north and anticyclonic flow to the southwest (Fig. 1d). However, since much of this reasoning employs comparisons with previous idealized solutions that might be complicated by strong background flows, we now systematically assess the response to separate mechanical and thermal forcings.

MECHANICALLY FORCED RESPONSE

We estimate the response to the mechanical influence of orography with a stationary wave model that has been used to study a range of orographically influenced circulations[14,23,24], but integrated here at finer resolu-

tion. We impose as a basic state the three-dimensional summer-mean flow from the FlatMex GCM, then use this model to find the adiabatic response to Mexico's orography (the forcing is the Control-FlatMex surface height anomaly).

This mechanically forced response consists of a meridional dipole in low-level vorticity, with a cyclone over much of the western US and an anticyclone southwest of Mexico (Fig. 2c). This structure strongly resembles the GCM response (Control-FlatMex; Fig. 2a), even though the GCM also includes diabatic feedbacks and any orographic thermal forcing. The stationary wave includes anomalous eastward flow upstream of and over the SMO, opposing the basic state trade winds, with a vertical structure and amplitude similar to that of the net GCM response (Fig. 2b, d). Between the surface and ~850 hPa, the total flow (basic state plus stationary wave anomaly) is eastward upstream of and over the SMO western slopes (orange contours in Fig. 2b, d). The stationary wave thus produces the time-mean upslope wind associated with core NAM moisture convergence and precipitation in this model (Extended Data Fig. 4) and observations[12].

The stationary wave is nonlinear, with isentropes (constant potential temperature surfaces) intersecting orography instead of bowing upward around it[25] (Fig. 2b, d; Extended Data Fig. 5 shows the linear response), but is straightforward to understand. When orography is high enough to block zonal winds, adiabatic flow, which in the time mean follows isentropes, must deviate northward or southward depending on where isentropes intersect the ground. In contrast with the regions and seasons used in prior studies of flow perturbed by narrow orography[25], peak temperatures in the NAM lie near 38°N, so isentropes over Mexico tilt downward to the north, intersecting the ground over the southwestern US (Fig. 2a, c, and Extended Data Fig. 6). Adiabatic zonal flow must thus ascend and turn southward as it encounters the SMO, because northward flow is blocked as it follows isentropes into the ground. Lower-resolution stationary wave solutions have a weaker anticyclone south of Mexico and give greater prominence to the northward Great Plains low-level jet (Extended Data Fig. 7a), perhaps explaining why orographic mechanical forcing has previously been more closely associated with that circulation[14].

SEASONAL AND DIURNAL THERMODYNAMIC MAXIMA

We now discuss how observations of strong diurnal and seasonal cycles of the thermodynamic state of the core NAM[12,11,13] are consistent with the hypothesis that
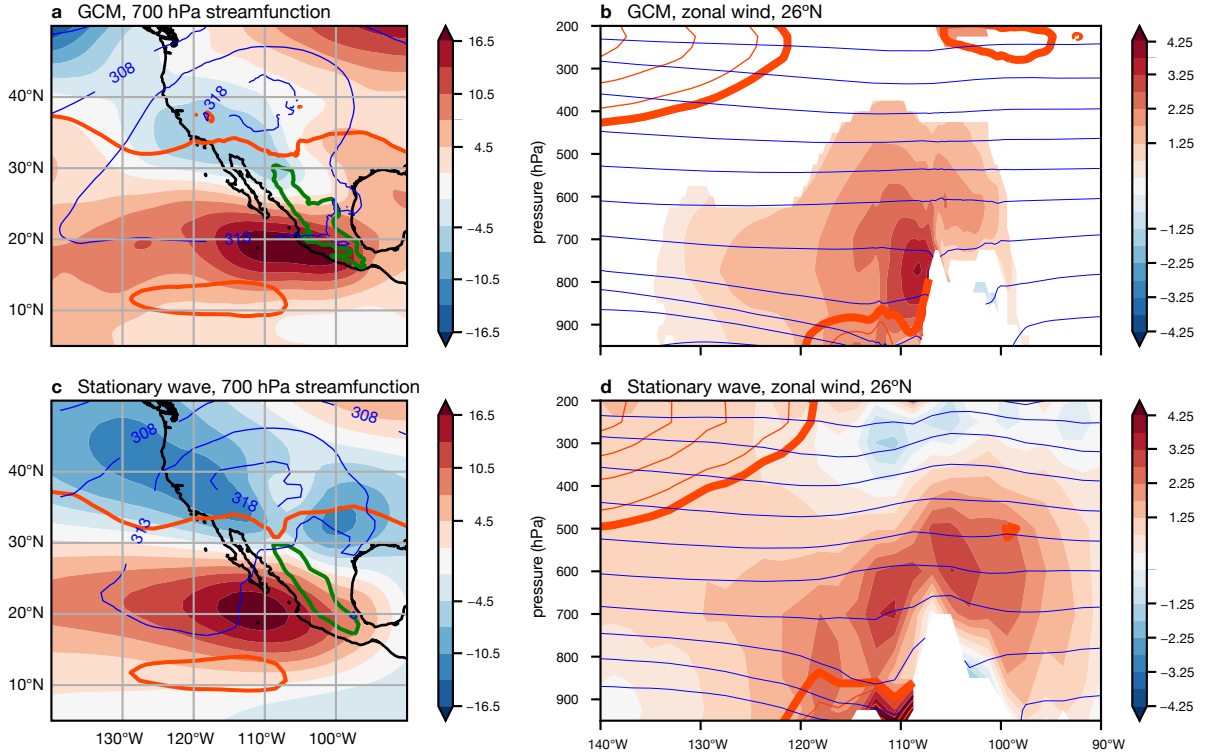
Figure 2. **Generation of eastward flow across western Mexico by the mechanically forced stationary wave.** Left panels show streamfunction of the anomalous 700 hPa horizontal wind (shading, in meters; air flows clockwise around maxima) for (a) the Control-FlatMex GCM integrations and (c) the stationary wave model forced by the Control-FlatMex surface height (1.5 km surface height is contoured in green). The thick orange line is the zero contour of the basic state zonal wind, which near $35°$N divides westward trade winds from prevailing eastward extratropical flow. Thin blue lines show 700 hPa potential temperature (in K). Right panels show anomalous zonal wind at $26°$N (shading, in m s^{-1}) for (b) the Control-FlatMex GCM, with only anomalies significant at the 5% level by a Student t-test plotted, and (d) the stationary wave model, both with isentropes plotted in blue (5 K contour interval) and orography masked in white; the total zonal wind (basic state plus response to orography) is contoured in orange, with a contour interval of 2 m s^{-1}, negative contours omitted, and zero contour in bold. Note the total wind is eastward at low levels west of the SMO. Streamfunction has been normalized by the gravitational acceleration and Coriolis parameter at $45°$N, giving it the units of geopotential height, and is not masked for statistical significance in (a) because of the nonlocal relation between streamfunction extrema and winds. Mapping software: Cartopy with Natural Earth shapefiles.

upslope flow and precipitation there are produced by a mechanically forced stationary wave. Moist convection requires both a reservoir of convective available potential energy (CAPE) and, typically, some lifting to overcome convective inhibition or release conditional instability. CAPE generally increases with h_s[26;27], and a large pool of air with high time-mean h_s lies over the Gulf of California and Gulf of Mexico (Fig. 1d). However, a strong diurnal cycle of h_s over land, caused by solar heating, produces a strong diurnal cycle of CAPE with a mid-afternoon peak over the western SMO (Fig. 3b; despite observational uncertainty, all estimates show high h_s over the western SMO with a large diurnal cycle over land). Thus, a warm and moist air layer from the Gulf of California flows eastward at low levels in the mechanically forced stationary wave, and its MSE is increased further by daytime surface heat fluxes while its tem-

perature drops adiabatically due to upslope flow, producing moist convection. Prior work[16] showed that the observed CAPE distribution does not explain why NAM precipitation favors the west coast of Mexico versus the east coast; release of CAPE through upslope flow in the stationary wave resolves this issue.

These effects can be synthesized by examining the seasonal cycle of h_s and near-surface zonal wind averaged in and upstream of the core NAM region, respectively. Upslope flow peaks in spring, before the observed rainy season, but h_s is low then so ample convective precipitation is not produced (Fig. 3c). Peak precipitation occurs a few months later when upslope flow is still strong and h_s has increased to its summer peak. Flattening Mexico's orography produces a slight increase in summer h_s, presumably because orography blocks the inland penetration of warm and moist oceanic air, yet

NAM precipitation decreases greatly as upslope flow is reduced (Fig. 1c). The seasonality of NAM precipitation thus seems to arise from the seasonal cycle in h_s (and CAPE) but, consistent with CAPE being a necessary but insufficient condition for convection, mechanically forced ascent in the stationary wave is needed to turn that thermodynamic seasonal cycle into rainfall.

The h_s distribution (Fig. 3a) also illustrates the deviation of NAM structure from that of classic tropical monsoons. In the latter we expect peak rainfall and peak low-level eastward wind on the equatorial side of the h_s maximum[28;29]. Instead, peak NAM rainfall occurs slightly east of (or even directly over) the peak h_s, and low-level eastward winds lie west of the peak h_s. This suggests that the classic, thermally forced tropical monsoon in North America consists of the oceanic precipitation maximum just south of Mexico, which would exist without Mexico's orography (Fig. 1c); southward deflection of prevailing extratropical winds by the SMO superimposes on that tropical monsoon the intense band of rainfall along Mexico's west coast (the core NAM).

RESPONSE TO A PURE THERMAL FORCING

We test the alternate hypothesis that the core NAM is primarily driven by thermal, rather than mechanical, orographic forcing using a third GCM integration in which the albedo of the surface that was flattened (most of Mexico) is reduced to 0.05 (FlatMexLowAlb). This provides a strong thermal forcing, with land albedo in much of the NAM region reduced below that of open ocean, yielding a local increase of about 20 W m^{-2} in the net energy input to the atmosphere (NEI; the sum of radiative and surface turbulent fluxes into each atmospheric column; Fig. 4a). In response, the high h_s region expands poleward and the oceanic precipitation maximum follows, expanding inland (compare Figs. 4b and 1c, d; Extended Data Fig. 9 shows anomalies). Anomalous low-level poleward flow over the region in which the albedo forcing was applied (Fig. 4a) is consistent with the Sverdrup balance achieved in the linear response to tropical thermal forcings[21]. As expected for a thermally forced tropical monsoon[28;29], peak rainfall lies on the equatorial side of the high-h_s region, and precipitation increases by about 2 mm day^{-1} over the broad region of the albedo forcing (Fig. 4b). The spatial structure of the response to the albedo forcing is highly distinct from the observed monsoon, with the former lacking both a precipitation maximum along Mexico's west coast and eastward flow extending 1,000 km west of the SMO.

SYNTHESIS AND IMPLICATIONS

The NAM is commonly categorized as a thermally forced tropical monsoon, with most previous work de-
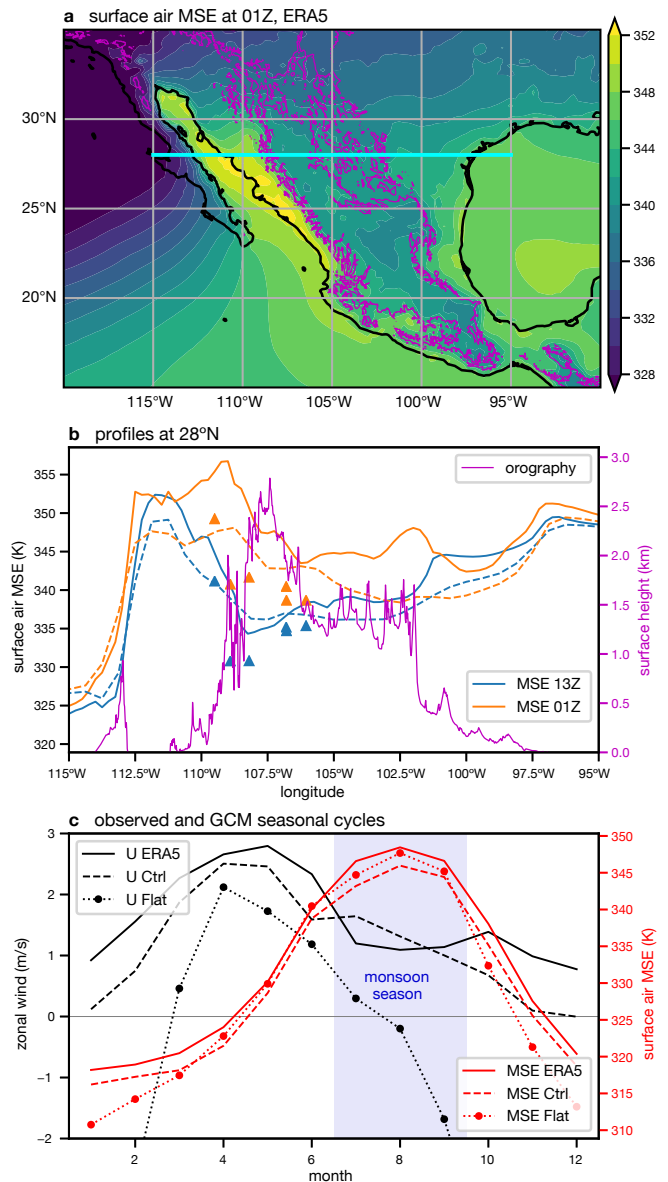

Figure 3. Diurnal and seasonal cycles in the North American monsoon. (a) Observed surface air moist static energy (MSE; shading, ERA5) at time of day when MSE peaks (6 pm local time in western Mexico), and orography (1.5 km surface height in magenta). Blue line marks zonal section used in (b), which shows peak MSE migrating from Gulf of California at 6 am (blue) to the western Sierra Madre at 6 pm (orange) local time. In (b), MSE is from ERA5 (solid lines) and MERRA-2 (dashed) reanalyses, and station data (triangles), indicating robustness in diurnal cycle amplitude and in location of maxima despite observational uncertainty. The section in (b) was taken at 28°N due to station data availability there, while wind sections in Fig. 2b, d were plotted at 26°N to be closer to center of the band of core NAM rainfall. (c) Seasonal cycle of surface air MSE averaged over NAM region (red lines) and near-surface zonal wind averaged over and upstream (i.e., west) of that region (black lines; Extended Data Fig. 8 shows averaging regions). Note large reduction in eastward flow and small increase in MSE during monsoon season when orography is flattened. Mapping software: Cartopy with Natural Earth shapefiles.

scribing it as either *(i)* similar to though smaller in scale than the South Asian monsoon[11], with a central role played by elevated plateau heating[3], or *(ii)* caused by land-ocean thermal contrast[30;4;25]. Our results suggest that core NAM precipitation instead requires mechanical forcing by the SMO, producing eastward, upslope flow that organizes convection to occur in a small part of a horizontally extensive pool of high-h_s air. The seasonal cycle of insolation generates that pool of high-h_s air in summer, with the diurnal cycle of insolation further enhancing h_s over coastal Mexico in afternoons. We expect mechanically forced stationary waves to be modified by moist convective heating, but the resemblance between horizontal winds in the adiabatic stationary wave solutions and in the moist GCM suggests this has only a modest effect on horizontal flow (Fig. 2).

These findings have implications for NAM variability in past and future climates, placing new emphasis on the jet stream and trade winds, and their interaction with orography. Accurate dynamical forecasts of NAM rainfall will require models with an unbiased jet stream and resolutions fine enough to represent the SMO. Thermodynamic controls on convection, long thought to dominate NAM rainfall, are important, but their representation in models should be evaluated in terms of how they affect convection in upslope flow. In contrast, surface conditions and convective stability over central Mexico may primarily affect the low amounts (1-2 mm day^{-1}) of summer rainfall received there. Finally, global climate change may alter the NAM through changes in both the extratropical jet stream and convective stability in regions of upslope flow, rather than through its influence on more general land-ocean thermodynamic contrasts.

METHODS

OBSERVATIONS

We obtain estimates of Earth's atmospheric state from ERA5, the fifth-generation atmospheric reanalysis from the European Centre for Medium-Range Weather Forecasts[31;32;33]. For years 1979-2019, we use ERA5 surface air temperature, surface air dewpoint (which we convert to specific humidity to calculate h_s), surface height, and 100-meter zonal wind. We also obtain surface air temperature, surface air dewpoint, and surface height from the Modern-Era Retrospective analysis for Research and Applications, version 2 (MERRA-2)[34;35]. Precipitation estimates are drawn from the Global Precipitation Measurement mission (GPM) Integrated Multi-satellitE Retrievals for GPM (IMERG),
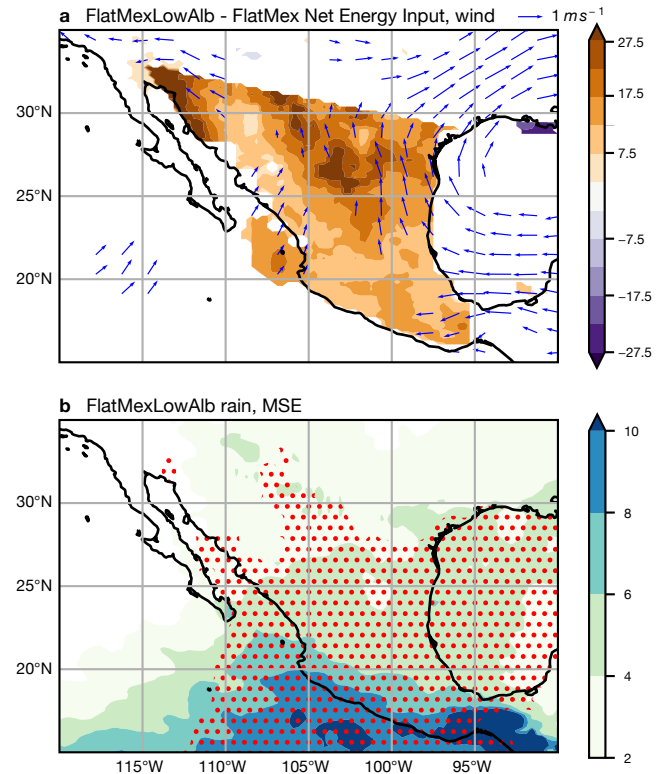

Figure 4. Response to a pure thermal forcing. (a) Anomalies, produced by imposing a reduced surface albedo in the GCM with flattened orography over Mexico, in 700 hPa horizontal wind (vectors) and net energy input through top and bottom boundaries of the atmosphere (shading, W m^{-2}). Anomalies are plotted only when statistically significant at the 5% level by a Student t-test (with wind anomalies plotted when either the zonal or meridional component is significant). (b) Total precipitation (shading; mm day^{-1}) and the extent of the region with high surface air moist static energy (defined as a 2-meter value larger than 345 K; red stippling) in the GCM with flattened orography and reduced albedo. Compare (b) with Fig. 1c, d to infer the MSE and precipitation response to the thermal forcing, or see Extended Data Fig. 9 for anomaly plots. Mapping software: Cartopy with Natural Earth shapefiles.

Final Precipitation L3 Daily 0.1 degree × 0.1 degree V06 product (GPM_3IMERGDF)[36]. We averaged years 2001-2020 to obtain the precipitation climatology shown in Fig. 1a. In addition to IMERG, we also use two land precipitation datasets to evalaute model performance over land: the Global Precipitation Climatology Centre (GPCC) dataset version 7, at 0.5° horizontal resolution[37;38], and the Climate Research Unit (CRU) gridded monthly rainfall from the University of East Anglia, version 3.24, at 0.5° horizontal resolution[39;40]. Plots of surface height use estimates from the ETOPO1 global relief model[41;42] at 1 arc-minute resolution; sur-

face height used in calculating reanalyzed h_s is taken from ERA5 and MERRA-2. All quantities are averaged July-September.

Surface air MSE is also computed for stations along a transect near 28°N using observations of temperature, specific humidity, and height from the North American Monsoon GPS Transect Experiment 2013[43] (measurements collected June-September 2013), and the 2017 North American Monsoon GPS Hydrometeorological Network[44] (hereafter referred to as GPS Hydromet 2017, measurements collected June-September 2017), which uses some of the permanent observation sites of the Trans-boundary, Land and Atmosphere Long-term Observational and Collaborative Network (TLALOCNet)[45]. Data from the GPS Transect Experiment 2013 are available every minute while GPS Hydromet 2017 are at 5-minute intervals. We compute h_s for all minutes within the 01 UTC and 13 UTC hours, corresponding to late afternoon and early morning in local time, respectively. We average for all days from July through September for both datasets, and retain only those stations for which there are less then ten days of missing data. Data for stations within 0.5° latitude of 28° were used for the transect. Changing the latitude of the MSE transect to 26°N, which was used for the wind sections in Fig. 2, does not change the qualitative results obtained from the reanalyses, although sufficient station data is not available at that latitude to conduct a comparison with direct observations.

MODELS

GLOBAL CLIMATE MODEL

Simulations were performed using the Community Atmospheric Model, version 5.1 (CAM5)[46] coupled to the Community Land Model, version 4[47], within the software infrastructure of the Community Earth System Model (CESM) version 2.1.3. We use the finite-volume dynamical core, which is typically configured with a horizontal resolution of 0.9° (latitude) by 1.3° (longitude); to better resolve the topography of the NAM region, we use a global horizontal resolution of 0.23° × 0.31° (i.e., approximately 25 km at the equator) with 30 vertical levels. We use the Sea ICE model (CICE) version 5 with prescribed ice cover and prescribed cyclic sea surface temperature (SST) from the year 2000. This model configuration is largely the same as that used in projections of the future behavior of tropical cyclones[48;49], and prior work has shown that the finer horizontal resolution used here improves the representation of the NAM in CAM5[19].

As discussed in previous work[50;17;18], climate models with relatively coarse horizontal resolution fail to resolve features like the Gulf of California and the Sierra Madres, thereby misrepresenting key NAM processes such as Gulf of California moisture surges[51;52;2], land-sea contrast[53], and mechanical flow-blocking by orography[54]. Furthermore, SST biases in coupled GCMs can have a detrimental impact on simulation of the NAM, biasing its seasonal evolution to produce a late withdrawal and thus an overly wet late summer and autumn[55;56;57]. Therefore, using a high resolution configuration with climatological SST reduces the model's bias and brings the regional circulation closer to observations (Extended Data Figs. 1-3).

To assess the influence of elevated terrain on the core NAM, we integrate the model with standard orography (Control) and again with flattened orography over most of Mexico (FlatMex). When flattening orography, we set both the surface height and the subgrid-scale standard deviation of orography to zero, with the latter used as input to both the vertically non-local subgrid-scale orographic gravity wave drag parameterization and the near-surface turbulent mountain stress scheme. In the integration with flattened orography over Mexico, we set surface height to zero within a quadrilateral having these vertices: (33°N, 245°E), (29°N, 265°E), (15°N, 257°E), and (15°N, 265°E). Orography on the Baja Peninsula is unaltered (it lies outside this quadrilateral). To avoid creating a high vertical wall of orography at the northern edge of this quadrilateral, where Mexico's orography joins the greater North American cordillera, the surface height is set to decrease linearly to zero over 2° of latitude immediately south of the northern edge of the quadrilateral; the same procedure is used for the subgrid-scale standard deviation of orography. To help distinguish between the thermal and mechanical influence of orography, we conduct a third integration in which the surface albedo of the flattened land is set to 0.05 (FlatMexLowAlb); this is done for both the direct and diffuse albedo by altering the land model (CLM4). This third integration has both flattened orography over Mexico and reduced surface albedo, in an attempt to impose an enhanced thermal forcing without the mechanical effects of orography. The spatial pattern of the albedo forcing does not exactly match the spatial pattern of orography because the albedo is uniformly set to 0.05 over the entire region where land was flattened; the effective forcing furthermore depends on the Control albedo rather than the Control terrain height. Nevertheless, the relatively weak magnitude and distinct spatial structure of the response to this albedo forcing (Fig. 4) suggest that further tuning would not greatly change the result. All three of the GCM configurations (Con-

trol, FlatMex, and FlatMexLowAlb) are run for 11 years of simulated time, with the last 10 years analyzed.

To understand how orography deflects the midlatitude westerlies toward the equator and then forces convection through upslope flow (Fig. 1), we analyze the time-mean zonal wind on a terrain-following level located within a typical subcloud layer (the atmospheric layer that lies below cloud base). For ERA5 we choose the level 100 m above Earth's surface, while for the GCM we use the horizontal wind on the third model level above the surface (level 957.5).

STATIONARY WAVE MODEL

To isolate the mechanical influence of Mexico's orography on the atmospheric circulation we use a fully nonlinear stationary wave model. The model was introduced by Ting and Yu (1998)[58], and solves the primitive equations in terms of vorticity, divergence, temperature, and the logarithm of surface pressure, using spherical harmonics[59;60;24]. Important distinctions with the GCM are that the stationary wave model *(i)* solves these equations for anomalies relative to a specific three-dimensional basic state and *(ii)* is adiabatic aside from a 15-day Newtonian relaxation of temperature toward the basic state, as used in prior work[58;61]. Transients, such as midlatitude baroclinic instabilities, are suppressed using drag and scale-selective diffusion. Specifically, interior Rayleigh drag on the anomalies is imposed with a 15-day time scale, with surface drag represented by gradually reducing this time scale to 0.3 days over the lowest 4 levels. Biharmonic diffusion with a coefficient of 10^{17} m^4 s^{-1} acts on vorticity, divergence, and temperature. The original version of this stationary wave model[58] was created with a rhomboidal truncation at wavenumber 15 (R15 spectral resolution) and 12 vertical levels. Later work integrated the model at R30 resolution with 14 vertical levels[23] and R30 resolution with 24 vertical levels[24]. We enhanced the resolution to R63 with 24 levels, based on code supplied by Isla Simpson. At R63, the model closely approximates the full width at half maximum height of the SMO when compared to ETOPO1 data and our CAM5 model, while this width was overestimated by more than 60% at R30.

The model was forced by imposing Mexico's orography on a basic state obtained by time-averaging the summer atmospheric state from the GCM without that orography. Specifically, we obtain the basic state by taking the 10-year July-September average atmospheric state from the FlatMex GCM run, and use the surface height difference between the Control and FlatMex GCM runs as the forcing. The stationary wave model nears a steady state after about 20 days, with the exception of the low-

est model level which drifts toward a steady state over about 60 days. Therefore, the model was run for 90 days of simulated time with the last 20 used for analysis. Linear stationary wave solutions were approximated, following previous work[62], by scaling the Control - FlatMex surface height forcing by 10^{-6} then multiplying the response by 10^6, thus rendering quadratic terms in the conservation equations a factor of 10^{-6} smaller than linear terms. The same integration and averaging periods were used for the linear solutions and for an integration of the model at the lower R30 resolution (Extended Data Figs. 5 and 7).

AUTHOR CONTRIBUTIONS

W.R.B conceived the study, devised and performed the GCM and stationary wave model integrations, and analyzed model output. S.P. assessed the GCM bias. Both authors analyzed observations and contributed to writing the manuscript.

COMPETING FINANCIAL INTERESTS

The authors declare no competing financial interests.

ADDITIONAL INFORMATION

Reprints and permissions information is available at www.nature.com/reprints. Correspondence and requests for materials should be addressed to W.R.B.

DATA AVAILABILITY

The ERA5 monthly averaged data by hour of day were downloaded from the Copernicus Climate Change Service Climate Data Store (identifiers cited in Methods). MERRA-2 and GPM data were downloaded from the

NASA Goddard Earth Sciences Data and Information Services Center (GES DISC; identifiers cited in Methods). ETOPO1 data were downloaded from the National Centers for Environmental Information at NOAA (identifiers cited in Methods). David K. Adams provided access to GPS Hydromet 2017, TLALOCNet, and GPS Transect Experiment 2013 data. The time-mean summer climatology from the GCM and time-mean output from the stationary wave model are archived at https://doi.org/10.5281/zenodo.5076509.

CODE AVAILABILITY

The CESM model, which is supported primarily by the National Science Foundation, was obtained from https://www.cesm.ucar.edu. Isla Simpson provided code for the stationary wave model, the original version of which was written by Mingfang Ting and Linhai Yu.

REFERENCES

[1] Douglas, M. W., Maddox, R. A., Howard, K. & Reyes, S. The Mexican Monsoon. *J. Climate* **6**, 1665-1677 (1993).

[2] Adams, D. K. & Comrie, A. C. The North American Monsoon. *Bulletin of the American Meteorological Society* **78**, 2197-2213. ISSN: 00030007. doi:10.1175/1520-0477(1997)078¡2197:TNAM¿2.0.CO;2 (1997).

[3] Tang, M. & Reiter, E. R. Plateau Monsoons of the Northern Hemisphere: A Comparison between North America and Tibet. *Mon. Wea. Rev.* **112**, 617-637 (1984).

[4] Vera, C. *et al.*. Toward a unified view of the American monsoon systems. *Journal of Climate* **19**, 4977-5000. ISSN: 08948755. doi:10.1175/JCLI3896.1 (2006).

[5] Mechoso, C. R., Robertson, A. W., Ropelewski, C. F. & Grimm, A. M. in *The Global monsoon system : research and forecast* (eds Chang, C.-P., Wang, B. & Lau, N.-C.) 197-206 (WMO/TD- No. 1266; Tropical Meteorology Research Programme (TMRP) Report- No. 70, 2005). doi:10.7916/D8ST803T.

[6] Bryson, R. A. & Lowry, W. P. Synoptic climatology of the Arizona summer precipitation singularity. *Bull. Amer. Meteor. Soc.* **36**, 329-339 (1955).

[7] Krishnamurti, T. N. Tropical east-west circulations during the northern summer. *J. Atmos. Sci.* **28**, 1342-1347 (1971).

[8] Broccoli, A. J. & Manabe, S. The effects of orography on midlatitude Northern Hemisphere dry climates. *J. Climate* **5**, 1181-1201 (1992).

[9] Stensrud, D., Gall, R., Mullen, S. & Howard, K. Model climatology of the Mexican monsoon. *J. Climate* **8**, 1775-1794 (1995).

[10] Schmitz, J. T. & Mullen, S. L. Water vapor transport associated with the summertime North American monsoon as depicted by ECMWF analyses. *J. Climate* **9**, 1621-1634 (1996).

[11] Johnson, R. H., Ciesielski, P. E., McNoldy, B. D., Rogers, P. J. & Taft, R. K. Multiscale variability of the flow during the North American Monsoon Experiment. *Journal of Climate* **20**, 1628-1648. ISSN: 08948755. doi:10.1175/JCLI4087.1 (2007).

[12] Berbery, E. H. Mesoscale Moisture Analysis of the North American Monsoon. *Journal of Climate* **14**, 121-137. ISSN: 0894-8755. doi:10.1175/1520-0442(2001)013¡0121:MMAOTN¿2.0.CO;2 (Jan. 2001).

[13] Nesbitt, S., Gochis, D. & Lang, T. The diurnal cycle of clouds and precipitation along the Sierra Madre Occidental observed during NAME-2004: Implications for warm season precipitation estimation in complex terrain. *Journal of Hydrometeorology* **9**, 728-743 (2008).

[14] Ting, M. & Wang, H. The Role of the North American Topography on the Maintenance of the Great Plains Summer Low-Level Jet. *J. Atmos. Sci.* **63**, 1056-1068 (2006).

[15] Wexler, H. A Boundary Layer Interpretation of the Low-level Jet. *Tellus* **13**, 368-378 (1961).

[16] Barlow, M., Nigam, S. & Berbery, E. Evolution of the North American Monsoon System. *J. Climate* **11**, 2238-2257 (1997).

[17] Collier, J. C. & Zhang, G. J. Effects of increased horizontal resolution on simulation of the North American monsoon in the NCAR CAM3: An evaluation based on surface, satellite, and reanalysis data. *J. Climate* **20**, 1843-1861 (2007).

[18] Pascale, S. *et al.*. The impact of horizontal resolution on North American monsoon Gulf of California moisture surges in a suite of coupled global climate models. *Journal of Climate* **29**, 7911-7936. ISSN: 08948755. doi:10.1175/JCLI-D-16-0199.1 (2016).

10

[19] Varuolo-Clarke, A. M., Reed, K. A. & Medeiros, B. Characterizing the North American Monsoon in the Community Atmosphere Model: Sensitivity to Resolution and Topography. *J. Climate* **32**, 8355-8372 (2019).

[20] Hu, S. & Boos, W. The physics of orographic elevated heating in radiative-convective equilibrium. *J. Atmos. Sci.* **74**, 2949-2965 (2017).

[21] Gill, A. E. Some simple solutions for heat-induced tropical circulation. *Quarterly Journal of the Royal Meteorological Society* **106**, 447-462. ISSN: 00359009. doi:10.1002/qj.49710644905 (1980).

[22] Rodwell, M. J. & Hoskins, B. J. Monsoons and the dynamics of deserts. *Quarterly Journal of the Royal Meteorological Society* **122**, 1385-1404. ISSN: 00359009. doi:10.1002/qj.49712253408 (1996).

[23] Simpson, I. R., Seager, R., Shaw, T. A. & Ting, M. Mediterranean summer climate and the importance of Middle East topography. *J. Climate* **28**, 1977-1996 (2015).

[24] Simpson, I. R., Seager, R., Ting, M. & Shaw, T. A. Causes of change in Northern Hemisphere winter meridional winds and regional hydroclimate. *Nat. Clim. Change* **6**, 65-70 (2016).

[25] Rodwell, M. J. & Hoskins, B. J. Subtropical Anticyclones and Summer Monsoons. *J. Climate* **14**, 3192-3211 (2001).

[26] Emanuel, K. A. *Atmospheric Convection* (Oxford University Press, 1994).

[27] Sobel, a. H. & Bretherton, C. S. Modeling tropical precipitation in a single column. *Journal of Climate* **13**, 4378-4392. ISSN: 08948755. doi:10.1175/1520-0442(2000)013¡4378:MTPIAS¿2.0.CO;2 (2000).

[28] Privé, N. C. & Plumb, R. A. Monsoon Dynamics with Interactive Forcing. Part II: Impact of Eddies and Asymmetric Geometries. *Journal of the Atmospheric Sciences* **64**, 1431-1442. ISSN: 0022-4928. doi:10.1175/JAS3917.1 (2007).

[29] Nie, J., Boos, W. R. & Kuang, Z. Observational evaluation of a convective quasi-equilibrium view of monsoons. *Journal of Climate* **23**, 4416-4428. ISSN: 08948755. doi:10.1175/2010JCLI3505.1 (2010).

[30] Higgins, R. W., Chen, Y. & Douglas, A. V. Interannual variability of the North American warm season precipitation regime. *Journal of Climate* **12**, 653-680. ISSN: 08948755. doi:10.1175/1520-0442(1999)012¡0653:ivotna¿2.0.co;2 (1999).

[31] Hersbach, H. *et al.*. The ERA5 global reanalysis. *Q J R Meteorol Soc.* **146**, 1999-2049. doi:10.1002/qj.3803 (2020).

[32] European Centre for Medium-Range Weather Forecasts. ERA5 Reanalysis (0.25 Degree Latitude-Longitude Grid). *Research Data Archive at the National Center for Atmospheric Research, Computational and Information Systems Laboratory. Updated monthly. Accessed 30 Apr 2020.*. doi:10.5065/BH6N-5N20 (2019).

[33] Hersbach, H. *et al.*. ERA5 monthly averaged data on single levels from 1979 to present. *Copernicus Climate Change Service (C3S) Climate Data Store (CDS). (Accessed on 25-Feb-2021)*. doi:10.24381/cds.f17050d7 (2019).

[34] Gelaro, R. *et al.*. The Modern-Era Retrospective Analysis for Research and Applications, Version 2 (MERRA-2).. *Journal of Climate* **30**, 5419-5454. ISSN: 0894-8755. doi:10.1175/JCLI-D-16-0758.1 (June 2017).

[35] Global Modeling and Assimilation Office (GMAO). *MERRA-2 tavgM_2d_slv_Nx: 2d,Monthly mean,Time-Averaged,Single-Level,Assimilation,Single-Level Diagnostics V5.12.4, Greenbelt, MD, USA, Goddard Earth Sciences Data and Information Services Center (GES DISC), Accessed: 1 March, 2021.* doi:10.5067/AP1B0BA5PD2K.

[36] Huffman, G., Stocker, E., Bolvin, D., Nelkin, E. & Tan, J. GPM IMERG Final Precipitation L3 1 day 0.1 degree x 0.1 degree V06. *Edited by Andrey Savtchenko, Greenbelt, MD, Goddard Earth Sciences Data and Information Services Center (GES DISC), Accessed: 03 May 2021* (ed Savtchenko, A.) doi:10.5067/GPM/IMERGDF/DAY/06 (2019).

[37] Schneider, U. *et al.*. GPCC's new land surface precipitation climatology based on quality-controlled in situ data and its role in quantifying the global water cycle. *Theoretical and Applied Climatology* **115**, 15-40 (2013).

[38] Schneider, U. *et al.*. *GPCC Full Data Monthly Product Version 7.0 at 0.5° : Monthly Land-Surface Precipitation from Rain-Gauges built on GTS-based and Historic Data. Accessed: 1 April 2020.* doi:10.5676/DWD_GPCC/FD_M_V7_050.

[39] Harris, I., Osborn, T. J., Jones, P. & Lister, D. Version 4 of the CRU TS monthly high-resolution gridded multivariate climate dataset. *Scientific Data* **7**, 109 (2020).

[40] The Centre for Environmental Data Analysis (CEDA) UK. *CRU TS4.00: Climatic Research Unit (CRU) Time-Series (TS) version 4.00 of high-resolution gridded data of month-by-month variation in climate, precipitation monthly means. Accessed: 3 April 2020* doi:10.5072/edf8febfdaad48abb2cbaf7d7e846a86.

[41] NOAA National Geophysical Data Center. ETOPO1 1 Arc-Minute Global Relief Model. *NOAA National Centers for Environmental Information. Accessed 14 Jan 2021* (2009).

[42] Amante, C. & Eakins, B. *ETOPO1 1 Arc-Minute Global Relief Model: Procedures, Data Sources and Analysis. NOAA Technical Memorandum NESDIS NGDC-24, Accessed 14 January 2021* tech. rep. (National Geophysical Data Center, NOAA, 2009). doi:10.7289/V5C8276M.

[43] Serra, Y. L. *et al.*. The North American Monsoon GPS Transect Experiment 2013. *Bulletin of the American Meteorological Society* **97**, 2103-2115 (2016).

[44] Pérez-Ruiz, E. R. *et al.*. Landscape Controls on Water-Energy-Carbon Fluxes Across Different Ecosystems during the North American Monsoon. *Journal of Geophysical Research: Biogeosciences* **126**, e2020JG005809. doi:https://doi.org/10.1029/2020JG005809 (2021).

[45] Cabral-Cano, E. *et al.*. TLALOCNet: A Continuous GPS-Met Backbone in Mexico for Seismotectonic and Atmospheric Research. *Seismological Research Letters* **89**, 373-381. ISSN: 1938-2057. doi:10.1785/0220170190 (Mar. 2018).

[46] Neale, R. B. *et al.*. Description of the NCAR Community Atmosphere Model (CAM 5.0).. *Ncar/Tn-464+Str.* doi:10.5065/D6N877R0. (2012).

[47] Oleson, K. W. *et al.*. *Technical Description of version 4.0 of the Community Land Model (CLM)* tech. rep. (NCAR Tech. Note NCAR/TN-478+STR, 2010), 257.

[48] Wehner, M. F. *et al.*. Resolution Dependence of Future Tropical Cyclone Projections of CAM5.1 in the U.S. CLIVAR Hurricane Working Group Idealized Configuration . *J. Climate* **28**, 3905-3925. doi:10.1175/JCLI-D-14-00311.1 (2015).

[49] Wehner, M. F., Reed, K. A., Loring, B., Stone, D. & Krishnan, H. Changes in tropical cyclones under stabilized 1.5 and 2.0° C global warming scenarios as simulated by the Community Atmospheric Model under the HAPPI protocols. *Earth Syst. Dynam.* **9**, 187-195. doi:10.5194/esd-9-187-2018 (2018).

[50] Mo, K. C., Juang, H. M. H., Higgins, R. W. & Song, Y. Impact of model resolution on the prediction of summer precipitation over the United States and Mexico. *J. Climate* **18**, 3910-3927. doi:10.1175/JCLI3513.1 (2005).

[51] Hales, J. E. Surges of maritime tropical air northward over the Gulf of California. *Mon. Wea. Rev.* **100**, 298-306 (1972).

[52] Brenner, I. S. A surge of maritime tropical air—Gulf of California to the southwestern United States. *Mon. Wea. Rev.* **102**, 375-389 (1974).

[53] Turrent, C. & Cavazos, T. Role of the land-sea thermal contrast in the interannual modulation of the North American Monsoon. *Geophys. Res. Lett.* **36**, L02808 (2009).

[54] Finch, Z. O. & Johnson, R. H. Observational analysis of an upper-level inverted trough during the 2004 North American Monsoon Experiment. *Mon. Wea. Rev.* **138**, 3540-3555 (2010).

[55] Liang, X., Zhu, J., Kunkel, K. E., Ting, M. & Wang, J. X. L. Do CGCMs simulate the North American monsoon precipitation seasonal-interannual variability? . *J. Climate* **21**, 4424-4448. doi:10.1175/2008JCLI2174.1 (2008).

[56] Geil, K. L., Serra, Y. L. & Zeng, X. Assessment of CMIP5 model simulations of the North American monsoon system. *J. Climate* **26**, 8787-8801 (2013).

[57] Pascale, S. *et al.*. Weakening of the North American monsoon with global warming. *Nature Climate Change* **7**. ISSN: 17586798. doi:10.1038/nclimate3412 (2017).

[58] Ting, M. & Yu, L. Steady response to tropical heating in wavy linear and nonlinear baroclinic models. *J. Atmos. Sci.* **55**, 3565-3582 (1998).

[59] Ting, M. & Held, I. M. The stationary wave response to a tropical SST anomaly in an idealized GCM. *J. Atmos. Sci.* **47**, 2546-2556 (1990).

[60] Ting, M. The stationary wave response to a tropical SST anomaly in an idealized GCM. *J. Atmos. Sci.* **51**, 3286-3308 (1994).

[61] Held, I. M., Ting, M. & Wang, H. Northern winter stationary waves: Theory and modeling. *Journal of Climate* **15**, 2125-2144. ISSN: 08948755. doi:10.1175/1520-0442(2002)015¡2125:NWSWTA¿2.0.CO;2 (2002).

[62] Hoskins, B. J. & Rodwell, M. J. A model of the Asian summer monsoon. Part I: The global scale. *Journal of the Atmospheric Sciences* **52**, 1329-1340. ISSN: 0022-4928. doi:10.1175/1520-0469(1995)052¡1329:AMOTAS¿2.0.CO;2 (1995).
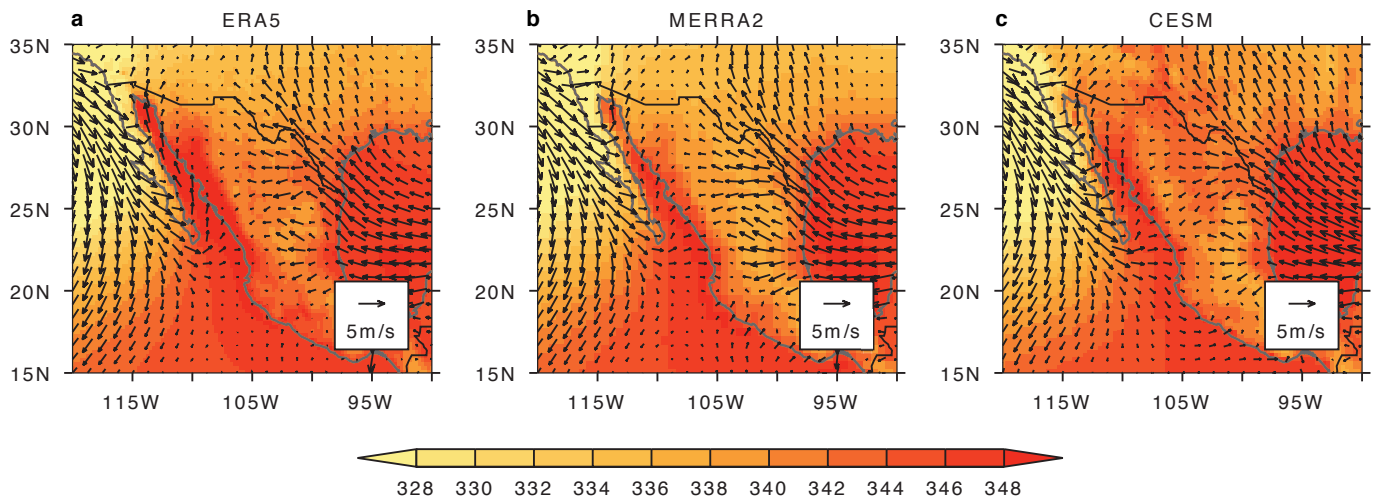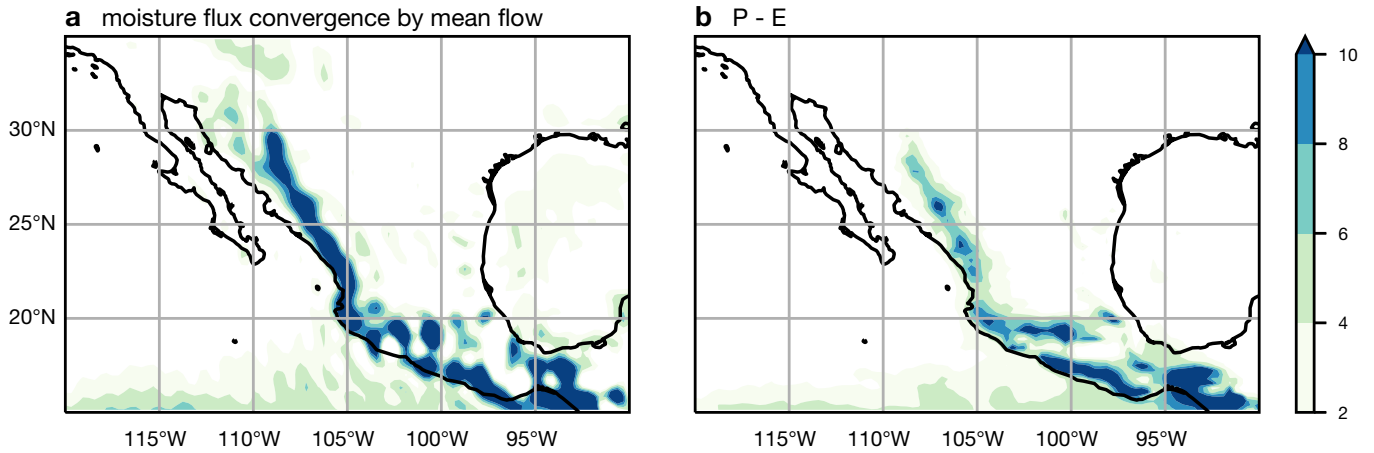
EXTENDED DATA FIGURES
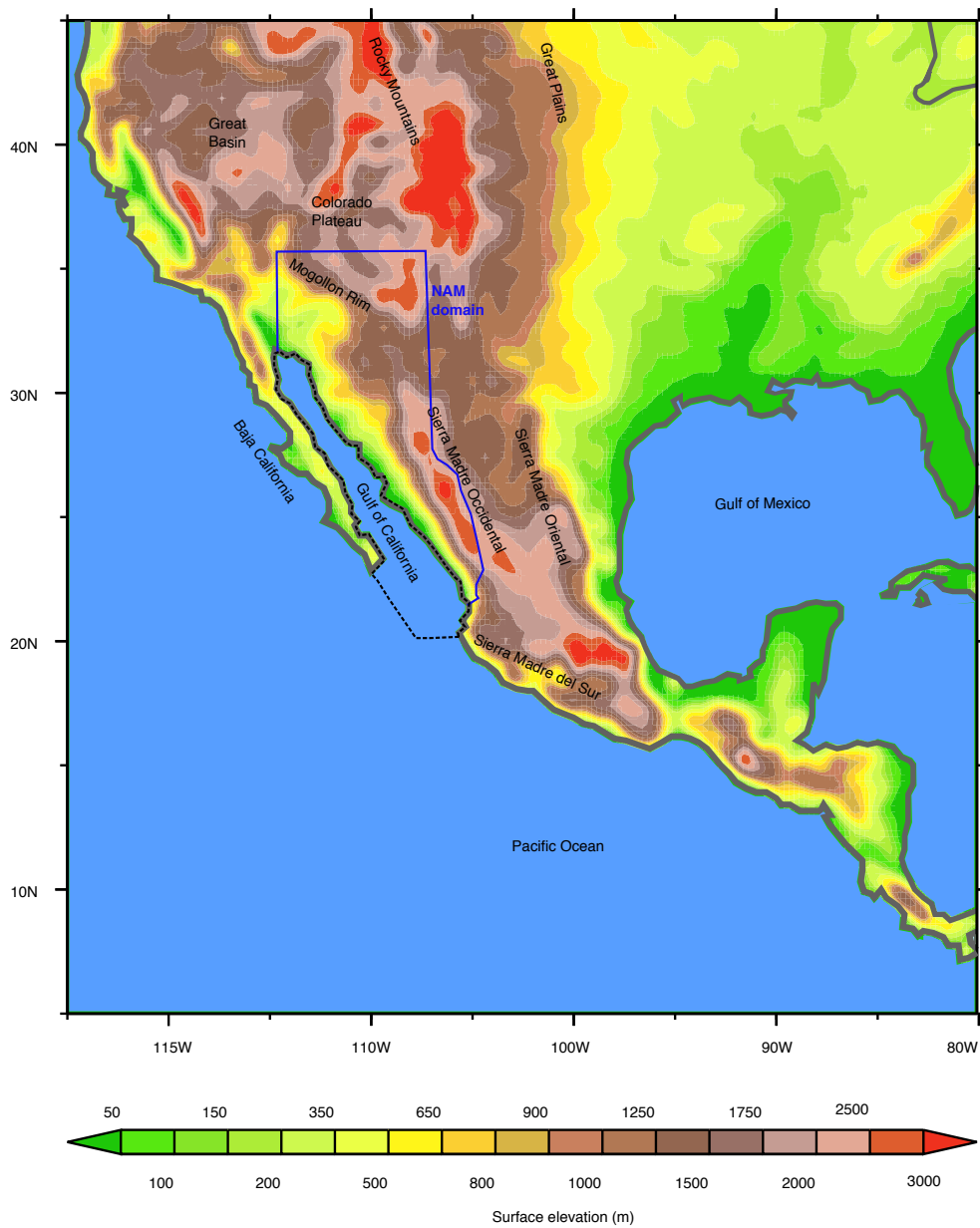
Extended Data Figure 1. Main geographic features of the North American monsoon. The blue line delimits land area used for area-averaging precipitation (NAM domain) in Extended Data Fig. 2a, while the dashed black curve outlines the Gulf of California region used for area-averaging the coast-parallel moisture flux in Extended Data Fig. 2b. Mapping software: IDL. Adapted from Pascale et al. (2017).
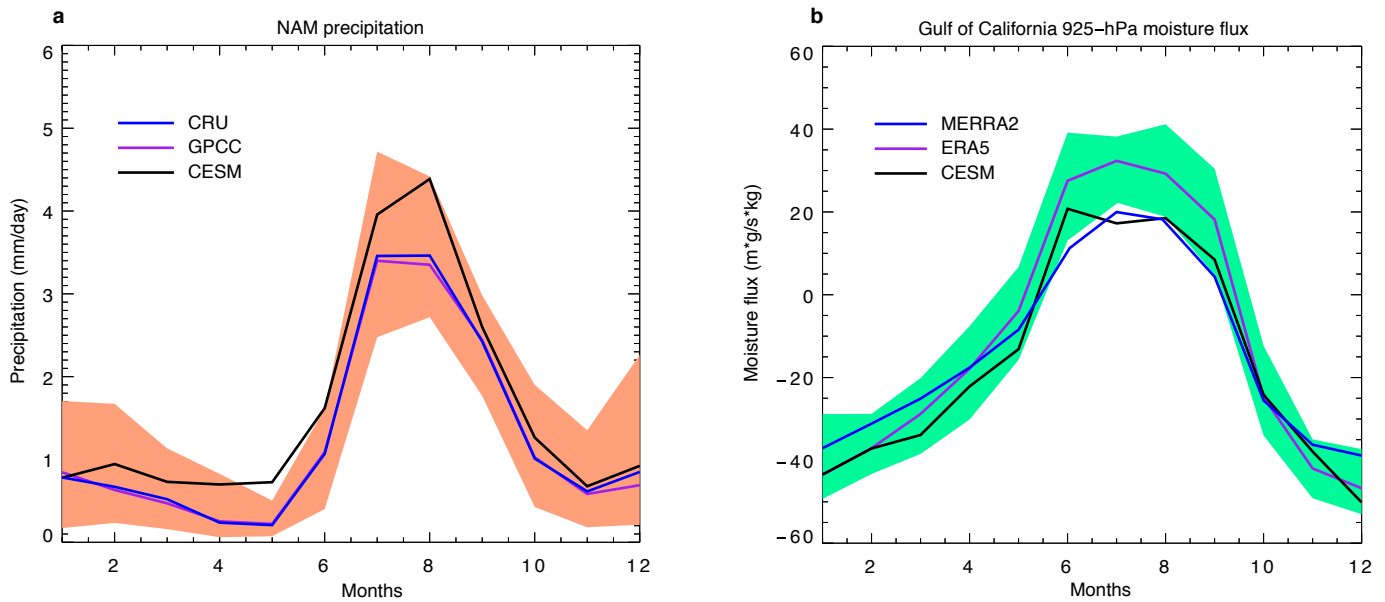
Extended Data Figure 2. Seasonal cycles of NAM precipitation and along-shore moisture flux in the Gulf of California (GoC) simulated by the high-resolution GCM largely fall within the range of observed interannual variability. a) Lines show the seasonal cycle of monthly precipitation averaged over the North American monsoon land domain (shown in Extended Data Fig. 1) and over the period 1980-2009 in two observational datasets (CRU in blue and GPCC in purple) and in the Control GCM (CESM; black). Shading bounds the 5th and 95th percentiles of GPCC interannual variability. The GCM lacks the large positive bias in autumn precipitation commonly seen in lower-resolution ocean-atmosphere coupled GCMs. b) Lines show the coast-parallel component of the 10-m moisture flux in the GoC for 1980-2009 in two reanalyses (MERRA2 in blue and ERA5 in purple) and the lowest model-level moisture flux in the Control GCM (CESM; black, about 7 hPa above the surface). Shading bounds the 5th and 95th percentiles of ERA5 interannual variability. The coast-parallel moisture flux is obtained by projecting the vector field along the coast-parallel direction (34° counterclockwise from north), then averaging over the Gulf of California domain shown in Extended Data Fig. 1.


Extended Data Figure 3. The high-resolution GCM captures the northward low-level wind and the tongue of high moist static energy (MSE) air over the Gulf of California. Vectors show 10-m horizontal wind from both a) ERA5 and b) MERRA2 (both 1980-2019 means), and c) the lowest model level wind from the Control GCM (CESM; roughly 7 hPa above the surface). Shading in all panels shows 2-m MSE, normalized by the specific heat of dry air to cast this variable in units of K. Mapping software: IDL.

Extended Data Figure 4. **Time-mean winds produce moisture convergence that balances precipitation in the Control GCM.** a) Vertically integrated moisture flux converged by summer-mean winds in the Control GCM, in mm day^{-1}. This has a highly similar spatial pattern to that of the summer-mean difference between precipitation and surface evaporation (b), which must closely approximate the total vertically integrated moisture flux convergence. The larger magnitude of (a) compared to (b) indicates that transient eddies dry the core NAM precipitation maximum. Convergence of the moisture flux was computed using spherical harmonics truncated at wavenumber 288 to reduce spectral ringing around orography. Mapping software: Cartopy with Natural Earth shapefiles.
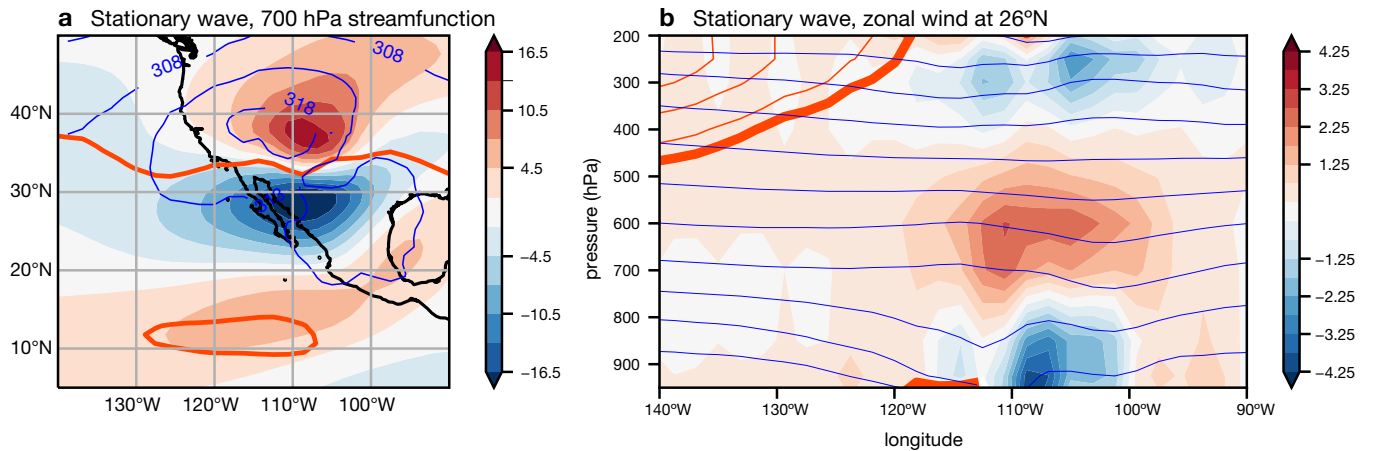

Extended Data Figure 5. **Linear stationary wave solution.** Linear solutions were obtained by scaling the Control - FlatMex surface height forcing by 10^{-6} then multiplying the response by 10^{6}, thus rendering quadratic terms in the conservation equations a factor of 10^{-6} smaller than linear terms. a) Streamfunction of anomalous 700 hPa horizontal wind (shading, in meters; air flows clockwise around maxima). The thick orange line is the zero contour of the basic state zonal wind, which near 35°N divides westward trade winds from prevailing eastward extratropical flow. Thin blue lines show 700 hPa potential temperature (in K). b) Anomalous zonal wind at 26°N (shading, in m s^{-1}) with isentropes plotted in blue (5 K contour interval); the total zonal wind (basic state plus response to orography) is contoured in orange, with a contour interval of 2 m s^{-1}, negative contours omitted, and zero contour in bold. Streamfunction in (a) has been normalized by the gravitational acceleration and Coriolis parameter at 45°N. Mapping software: Cartopy with Natural Earth shapefiles.

FlatMex u, θ, 257°E
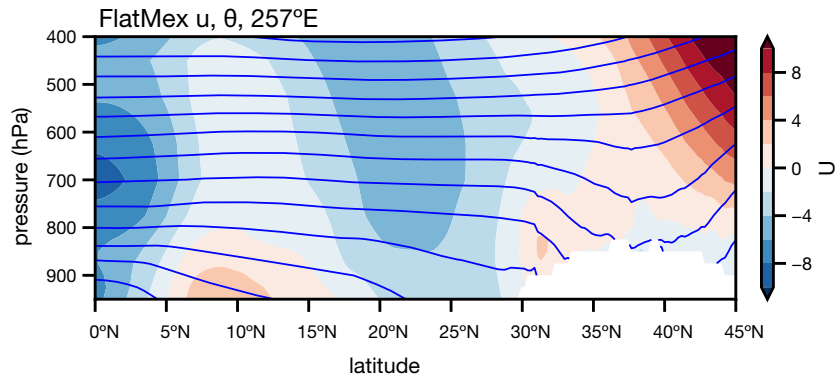
Extended Data Figure 6.   Basic state isentropes and zonal wind, illustrating how steady, lower-tropospheric adiabatic flow must be deflected southward to avoid being blocked by the ground. Summer-mean zonal wind (shading, m s^{-1}) and potential temperature (blue contours, interval 5 K) at 103°W in the FlatMex integration. Orography is masked in white.

a Stationary wave, 700 hPa streamfunction

b Stationary wave, zonal wind at 26°N
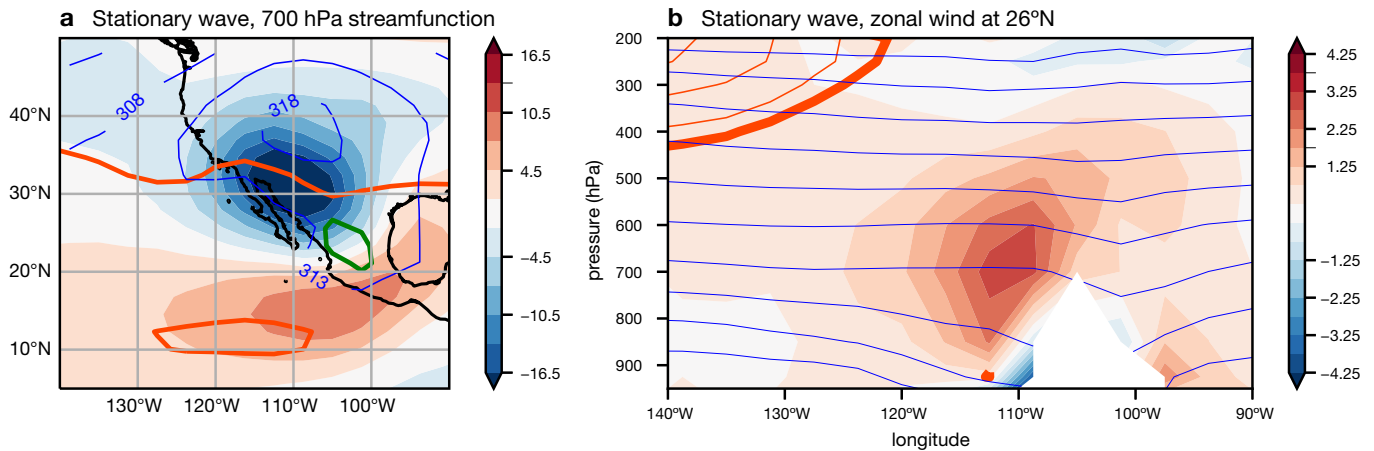
Extended Data Figure 7.   Low-resolution stationary wave solution. Fully nonlinear response to the Control - FlatMex surface height forcing obtained with the stationary wave model integrated at R30 horizontal resolution (main text Fig. 2c, d showed solutions at R63 resolution). a) Streamfunction of anomalous 700 hPa horizontal wind (shading, in meters; air flows clockwise around maxima). Surface height of 1.5 km is contoured in green, and thick orange line is zero contour of basic state zonal wind, which near 35°N divides westward trade winds from prevailing eastward extratropical flow. Thin blue lines show 700 hPa potential temperature (in K). b) Anomalous zonal wind at 26°N (shading, in m s^{-1}) with isentropes plotted in blue (5 K contour interval) and orography masked in white; the total zonal wind (basic state plus response to orography) is contoured in orange, with a contour interval of 2 m s^{-1}, negative contours omitted, and the zero contour in bold. Streamfunction in (a) has been normalized by the gravitational acceleration and Coriolis parameter at 45°N. Note that total near-surface flow just west of the SMO is westward, unlike in the high-resolution solutions shown in Fig. 2d. Mapping software: Cartopy with Natural Earth shapefiles.
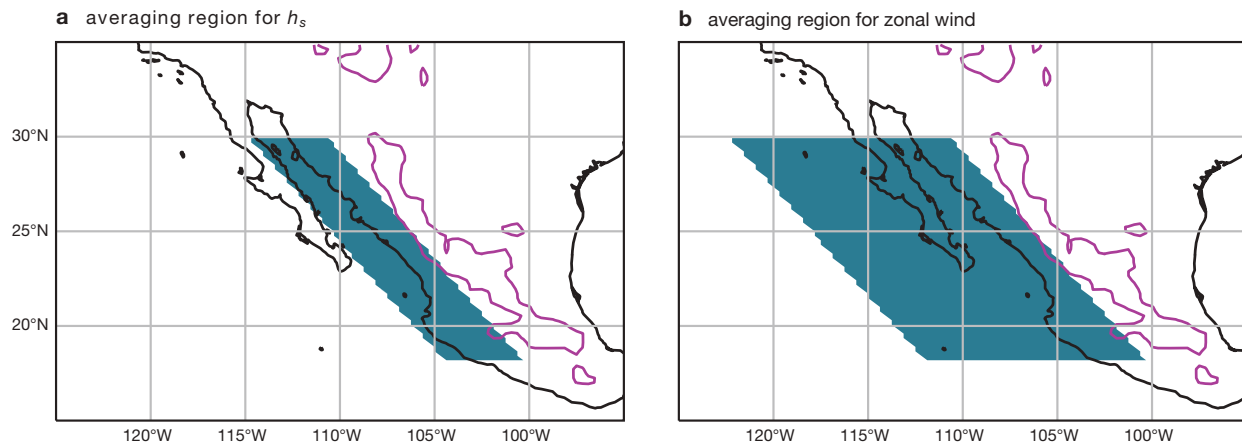
Extended Data Figure 8. **Averaging regions for the seasonal cycle of MSE and wind shown in main text Fig. 3c**. Regions over which a) surface air MSE and b) low-level zonal wind were averaged in our seasonal cycle diagnostics. Mapping software: Cartopy with Natural Earth shapefiles.
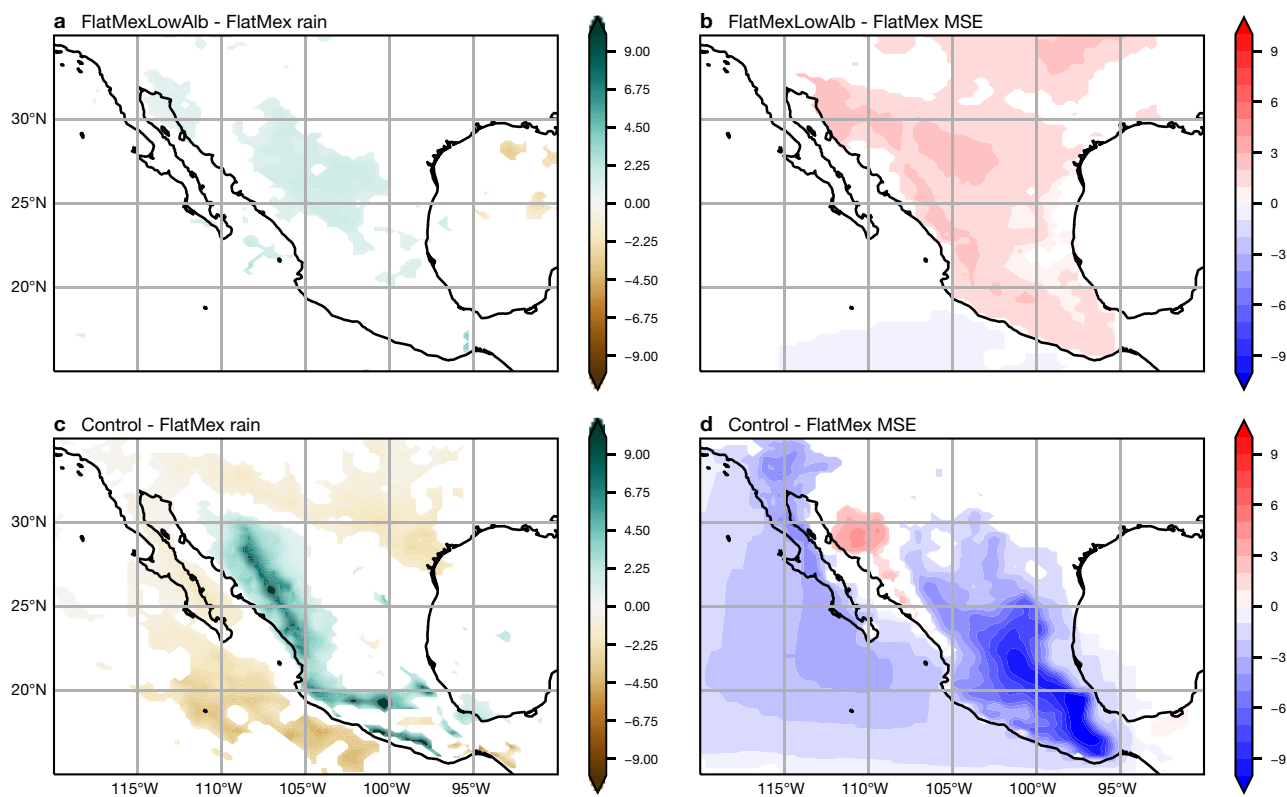
Extended Data Figure 9. **Distinct spatial structure of the response to the pure thermal forcing.** Anomalies in summer-mean a) precipitation (mm day^{-1}) and b) surface air MSE (K) in the FlatMexLowAlb model run relative to the FlatMex run. Panels (c) and (d) show the same as (a) and (b) but for the Control run relative to FlatMex. In all panels, only anomalies that are statistically significant at the 5% level by a Student t-test are shown. Mapping software: Cartopy with Natural Earth shapefiles.